Journal of Applied Mechanics Vol.13, pp.253-262 (August 2010) JSCE

Simulation of Dynamic Crack Growth in Shock Wave Lithotripsy with PDS-FEM

M. L. L. Wijerathne*, Muneo Hori**, Hide Sakaguchi***

*Ph.D., Center for Sustainable Urban Regeneration, University of Tokyo (7-3-1 Hongo, Bunkyo, Tokyo, 113-8656)
**Ph.D., Earthquake Research Institute, University of Tokyo (1-1-1 Yayoi, Bunkyo, Tokyo, 113-0023)
***Ph.D., IFREE, Japan Agency for Marine-Earth Science and Technology (Yokohama Institute of Earth Sciences, 3173-25 Showa-machi, Kanazawa-ku, Yokohama, 236-0001)

A set of Shock Wave Lithotripsy(SWL) related experimental observations including 3D dynamic crack propagation, reported in literature, are simulated with the aim of understanding the fragmentation of kidney stone with SWL. Extracorporeal shock wave lithotripsy (ESWL) is the fragmentation of kidney stones by focusing an ultrasonic pressure pulse onto the stones. 3D models with fine discretization are used to accurately capture the high amplitude shear shock waves, which play an important role in kidney stone fragmentation. For solving the resulting large scale dynamic crack propagation problem, PDS-FEM is used since it provides numerically efficient failure treatments. With a distributed memory parallel code of PDS-FEM, experimentally observed 3D photoelastic images of transient stress waves and crack patterns in cylindrical samples are reproduced. The experimental and numerical crack patterns are quantitatively in agreement. The results confirm that the high amplitude shear waves induced in solid play a key role in stone fragmentation.

Key Words : *Shock wave lithotripsy, Dynamic crack propagation, PDS-FEM*

1. Introduction

Extracorporeal shock wave lithotripsy (ESWL) is the fragmentation of kidney stones (urinary calculosis) by focusing an ultrasonic pressure pulse onto the stones. With repetitive application of ultrasonic pulses, stones are broken into small enough pieces which can pass naturally through the urinary system. Currently, a significant percentage of kidney stone patients are treated with this nearly three decades old method[1),2)]. Despite it's wide usage, the mechanism of stone fragmentation has not been well understood[1),3),4)]. Consequently, modern day SWL instruments are not much different from the oldest design, except for the ease of clinical usage[2)].

To further enhance the SWL technology, it is necessary to understand how the stress waves induced in stones initiate cracks, how the stress waves interact with extending crack surfaces and where the resulting high stress regions appear. 2D ray tracing techniques and high speed photoelasticity have been used to locate the high stress regions where the crack initiation could occur[3)]. Being all the dimensions comparable in sizes, the induced state of stress in kidney stones are fully 3D. Up-to-date, no methods have been found to evaluate 3D stress distribution from 3D photoelastic images. Due to the lack of experimental techniques to measure full field dynamic state of stress, numerical simulations are the only way to quantitatively analyze the state of stress, crack initiation and propagation in kidney stones. Up-to-date, no successful simulation of SWL stone fragmentation, in 3D, has been reported. Almost all the reported numerical simulations of SWL are limited to studying lithotriptor shock wave and stone interaction with simplified 2D models[1),4)].

In this study, some of the SWL related experimental observations published in literature by Xi et al.[3)] have been numerically reproduced in 3D, including dynamic crack propagation. With a series of experiments, Xi et al.[3)] have captured images of transient stress waves of various sizes and shapes of epoxy samples as 3D photoelastic images and studied the crack patterns in plaster of Paris samples of various sizes and shapes. In some literature, simplified 2D numerical models have been qualitatively validated by comparing those 3D photoelastic images with displacement or stress field [1),2)]. Unlike those, in this study, experimental 3D photoelastic images are compared with numerically calculated photoelastic images. Due to the lack of information, only a qualitative comparison is done. Good agreement of numerical and experimental photoelastic images validates the numerical model used in this study. One of the interesting results reported by Xi et al. is T-shaped crack patterns in cylindrical plaster of Paris samples, when exposed to multiple lithotriptor shock waves. These T-shaped crack patterns are simulated and the experimental and numerical crack patterns are found to be in agreement, quantitatively. Cleveland et at.[1], have reported that the induced shear waves are of high amplitude and could be playing a major role in stone breaking. Our results also confirm that induced high amplitude shear waves are mainly responsible for the crack formation.

A recently developed variant of FEM called PDS-FEM[5),6)], is used in this study since its failure treatment is numerically efficient even to simulate crack propagation in large scale problems. The lithotriptor shock wave has nearly $2\mu s$ high compression phase and the shear shock waves induced in the solid are spatially narrow. Both these features play an important role in SWL. To accurately capture these features, the numerical model has to be discretized to large number of elements. In this study, the domain was discretized to 11.2 million tetrahedral elements. To model 3D crack propagation in such large models, numerical methods with numerically efficient failure treatments have to be used. Common FEM approaches like re-meshing, element/nodal enrichment, etc. involves numerically intensive treatments for creating a new crack surface. Compared to these traditional approaches, the failure treatment of PDS-FEM is light enough to simulate 3D crack propagation in large scale problems[6)]. A distributed memory parallel program of PDS-FEM was used to simulate this large scale 3D dynamic crack propagation problem.

The rest of the paper is organized as follows. For the sake of completion, formulation of PDS-FEM and its dynamic extension are briefly explained in section 2. In section 3, a brief explanation of the experiments reported by Xi et al., problem setting for the numerical simulations and implementation of solid fluid interaction are presented. Comparison of numerical and experimental results of 3D photoelastic images and crack patterns are given in section 4. Finally, a short summery is given in the last section.

2. Numerical Method for Modeling Dynamic Crack Propagation: PDS-FEM

PDS-FEM is based on a non-conventional discretization scheme called *particle discretization scheme* (PDS), which uses a set of non-overlapping characteristic functions of two conjugate geometries to discretize functions and their derivatives. The non-overlapping shape functions introduce numerous discontinuities to the discretized function, all over the domain. Solving a growing crack problems with PDS-FEM is numerically efficient since the discontinuities in the discretized displacement field can be utilized to model growing crack surfaces. Detailed formulation of PDS and PDS-FEM is given in reference [5),6)] and only a brief description on PDS, PDS-FEM and its dynamic extension are given in the rest of this section.

Throughout this paper, the Cartesian coordinates system and the index notation (i.e., x_i stands for the i^{th} coordinate) are used. We use the summation convention and an index following a comma stands for the partial differentiation with respect to the corresponding coordinate.

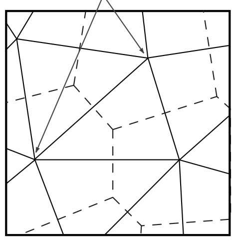

Fig. 1 2D Conjugate geometries used in PDS

2.1 Particle discretization scheme (PDS)

PDS uses characteristic functions of a pair of conjugate geometries, hypo-Voronoi and Delaunay tessellations, to discretize functions and their derivatives. First the domain of analysis is discretized with hypo-Voronoi and Delaunay tessellations. For a given set of mother points $\{\mathbf{x}^\alpha\}$ in 2D, the hypo-Voronoi diagrams are obtained by first forming the Voronoi tessellation and then moving the common meeting point of neighbouring three Voronoi diagrams to the centre of gravity of the triangle, formed by the three mother points of the Voronoi diagrams(see Fig. 1). With a similar process, 3D hypo-Voronoi diagrams can be generated.

Using the set of characteristic functions $\phi^\alpha(\mathbf{x})$ of hypo-Voronoi diagrams $\{\Phi^\alpha\}$'s, PDS discretizes a function f defined over a domain B as $f^d = \sum_\alpha f^\alpha \phi^\alpha(\mathbf{x})$. To circumvent the problem of unbounded derivatives of the approximation f^d (i.e. $f^d_{,j} = \frac{\partial f_d}{\partial x_j}$ is zero inside Φ^α's and is unbounded along the boundaries $\partial\Phi^\alpha$'s), an average value $f,^d_j$ is calculated using the Delaunay tessellation associated with Voronoi diagrams, Ψ^β. Using the set of characteristic functions of the Delaunay tessellation $\left\{\Psi^\beta\right\}$, $f_{,i}$ is discretized as $f^d_{,i} = \sum g^\beta_i \psi^\beta(\mathbf{x})$. Discretization of functions and their derivatives, with the characteristic functions of a pair of conjugate geometries is the essence of PDS.

2.2 PDS-FEM

Implementation of PDS in FEM framework to solve the boundary value problems of continuum is called PDS-FEM. We consider the implementation of PDS-FEM to solve the boundary value problem of linear elastic continuum, assuming infinitesimal deformations. As customary, the boundary value problem is posed as

$$\begin{cases} (c_{ijkl}(\boldsymbol{x})u_{k,l}(\boldsymbol{x}))_{,i} + b_j(\boldsymbol{x}) = \rho(\boldsymbol{x})\ddot{u}_j(\boldsymbol{x}) & \text{in } B, \\ u_i(\boldsymbol{x}) = \overline{u}_i(\boldsymbol{x}) & \text{on } \partial B. \end{cases} \tag{1}$$

Here, c_{ijkl} is heterogeneous linear elasticity tensor, ρ is the density, b_i and $\bar{u}_i$ are the body forces and displacements prescribed in the body B and on the boundary ∂B, respectively. Also, the standard notation of dots over a variable is used to denote derivatives with respect to time. PDS-FEM uses the following functional of displacements, strain($\boldsymbol{\epsilon}$) and stress($\boldsymbol{\sigma}$) to transform the above strong form of the governing equations to an equivalent variational problem.

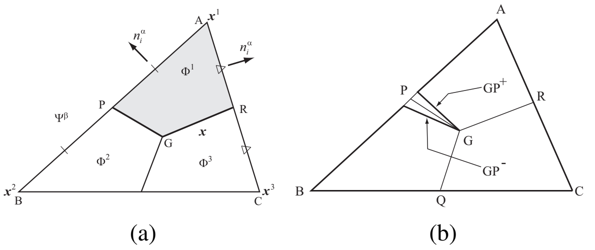

Fig. 2 Evaluation of $b_j^{\beta\alpha}$ and approximate treatment of a crack growing along Voronoi block boundary PG

$$I = \int_B \frac{1}{2}\epsilon_{ij}c_{ijkl}\epsilon_{kl} - \sigma_{ij}(\epsilon_{ij} - u_{j,i}) + b_i u_i - \frac{1}{2}\rho\dot{u}_i\dot{u}_i \, \mathrm{d}s.$$

It is straightforward to show that Eq. (1) can be derived by setting the first variation of the above functional $\delta I(\boldsymbol{u}, \boldsymbol{\epsilon}, \boldsymbol{\sigma}) = 0$.

Applying the PDS, the linear elastic domain B is discretized with hypo-Voronoi diagrams and associated Delaunay tessellation. Displacement field u_i and body forces b_i are discretized with the set of characteristic functions $\{\phi^\alpha\}$ as $u_i(\boldsymbol{x}) = \sum_\alpha u_i^\alpha \phi^\alpha(\boldsymbol{x})$ and $b_i(\boldsymbol{x}) = \sum_\alpha b_i^\alpha \phi^\alpha(\boldsymbol{x})$. The variables associated with derivatives σ_{ij}, ϵ_{ij} are discretized in terms of $\{\psi^\beta\}$ as $\sigma_{ij}(\boldsymbol{x}) = \sum_\beta \sigma_{ij}^\beta \psi^\beta(\boldsymbol{x})$, $\epsilon_{ij}(\boldsymbol{x}) = \sum_\beta \epsilon_{ij}^\beta \psi^\beta(\boldsymbol{x})$. The linear elasticity tensor is discretized with $\{\psi^\beta\}$ as $c_{ijkl}(\boldsymbol{x}) = \sum_\beta c_{ijkl}^\beta \psi^\beta(\boldsymbol{x})$. Substituting these discretized forms to I and setting the first variation to zero, the discretization coefficients are determined as $\sigma_{ij}^\beta = c_{ijkl}^\beta \epsilon_{kl}^\beta$ and $\epsilon_{ij}^\beta = \sum_\alpha b_i^{\beta\alpha} u_j^\alpha$, where

$$b_j^{\beta\alpha} = \frac{1}{\Psi^\beta} \int_{\Psi^\beta} \phi^\alpha{}_{,j}(\boldsymbol{x}) \, \mathrm{d}s. \tag{2}$$

Although $\phi,_j^\alpha$'s are unbounded along the boundary $\partial\Phi^\alpha$, an average value over Ψ^β can be calculated using the Gauss theorem. As an example, it is straightforward to obtain $b_i^{\beta 1} = \frac{1}{2\Psi}\varepsilon_{ij3}(x_j^2 - x_j^3)$ (see Fig. 2a). Expressions for $b_i^{\beta 2}$ and $b_i^{\beta 3}$ can be obtained by suitably replacing the superscripts. Substituting these results to the discretized I and setting $\partial I / \partial u_i^\alpha = 0$, we obtain a set of linear equations for $\{\boldsymbol{u}^\alpha\}$, as

$$\sum_{\alpha'} k_{ij}^{\alpha\alpha'} u_j^{\alpha'} - \Phi^\alpha b_i^\alpha = m^\alpha \ddot{u}_i^\alpha, \tag{3}$$

where the element stiffness matrix

$$k_{ij}^{\alpha\alpha'} = \sum_\beta \Psi^\beta c_{ikjl}^\beta b_k^{\beta\alpha} b_l^{\beta\alpha'}. \tag{4}$$

Eq. (3) is the governing matrix equation of FEM implemented with PDS, i.e., PDS-FEM. When the hypo-Voronoi mother points, $\{x^\alpha\}$, are considered as nodes and Delaunay tessellations are considered as elements, the element stiffness matrix of PDS-FEM is exactly equal to that of FEM with linear elements, numerically. Therefore, PDS-FEM has the same accuracy of FEM at nodal points. Extension of PDS-FEM to higher dimensions is straightforward with hypo-Voronoi diagram and the associated Delaunay tessellation of the relevant dimension.

2.3 Approximate Failure Treatment of PDS-FEM

With PDS-FEM, the existing discontinuities in the discretized displacement field can be easily utilized to model propagating cracks. Even though homogeneous material properties are assumed, forcing cracks to propagate along the hypo-Voronoi boundaries makes the numerical model to be heterogeneous with respect to material strength; hypo-Voronoi blocks have infinite strength while their boundaries have a finite strength. This feature of PDS-FEM is useful in kidney stone fragmentation simulations and other crack propagation analysis of real materials. Different kidney stone samples, with the same geometry, break with different crack profiles due to their heterogeneous material properties. With PDS-FEM, the presence of these material heterogeneity can be easily simulated by choosing different arrangements of Voronoi tessellations which corresponds to different distributions of material strength.

The approximate failure treatment is formulated as changes in elastic tensor c_{ijkl}. When a Voronoi block boundary is broken under tension, it is modelled by setting $c_{ijkl} = 0$ in an infinitesimally thin neighbourhood, $\mathrm{GP^+P^-}$, of the broken Voronoi block boundary , while c_{ijkl} is unchanged in the rest of the domain (see Fig. 2b). This changes the element stiffness matrix Eq. (4) of the broken element [1]. This change of $k_{ij}^{\alpha\alpha'}$ is due to the fact that $b_i^{\beta\alpha}$, given by Eq. (2), drops the contribution from the derivative of the Voronoi characteristic function that appears in $\mathrm{GP^+P^-}$. A crack along GP can be modelled by recomputing the element stiffness matrix with the changed $b_i^{\beta\alpha}$'s and updating the global stiffness matrix. The numerical overhead associated with this approximate treatment is almost equal to re-computation of an element stiffness matrix. Hence, PDS-FEM failure treatment is numerically efficient compared to other FEM treatments.

2.4 Time integration

For the time integration of Eq. (3), any standard time integration method like Newmark-beta, Verlet methods, asynchronous variational integrators[7)], etc. can be employed. In addition to these standard algorithms in solid mechanics, there is a rich set of symplectic, energy momentum preserving algorithms used in molecular dynamics and celestial mechanics[8),9),10)]. These algorithms for simulating Hamiltonian flows are higher order accurate, explicit, have a good behaviour in long time integrations and can deal with steep potentials. As explained below, the last property is important in crack propagation simulations. Because of these attractive properties, we implemented such algorithm for time integration of Eq. (3).

[1] A Delaunay polyhedron containing one or more broken hypo-Voronoi boundary is referred as a broken element.

The domain discretized with PDS can be interpreted as modelling a continuum with a collection of particles; according to the Eq. (3), the non-overlapping shape functions result in lumped masses or isolated particles at Voronoi mother points $\{\mathbf{x}^\alpha\}$. The interaction of these particles is defined by the stiffness matrix. Even though, for infinitesimal deformations, the inter particle interactions defined by the Eq. (4) are linear, propagating cracks bring drastic changes. We implemented the bi-lateral symplectic algorithm by Lappo Casetti[10] for time integration of Eq. (3) since it is suitable for problems with steep potentials.

Denoting the mass and velocity of hypo-Voronoi block Φ^α with m^α and $\dot{u}_i^\alpha$, the Lagrangian for the collection of interacting particles can be written as $L = \sum_\alpha \frac{1}{2} m^\alpha \dot{u}_i^\alpha \dot{u}_i^\alpha - \sum_\alpha \left[\frac{1}{2} K_{ij}^{\alpha\alpha'} u_j^\alpha u_i^{\alpha'}\right]$. Hamiltonian for this collection of particles is $H = p\dot{q} - L$, where q and $\dot{q}$ are generalized coordinate and generalized velocity. Since our coordinate system is stationary $q_i^\alpha = u_i^\alpha$, $\dot{q}_i^\alpha = \dot{u}_i^\alpha$ and the generalized momentum are $p_i^\alpha = \frac{\partial L}{\partial \dot{q}_i^\alpha} = m^\alpha \dot{u}_i^\alpha$. The system of Hamiltonian equations for the set of particles$\{\Phi^\alpha\}$ are $\dot{q}_i^\alpha = \frac{\partial H}{\partial p_i^\alpha} = \frac{p_i^\alpha}{m^\alpha}$ and $\dot{p}_i{}^\alpha = -\frac{\partial H}{\partial q_i^\alpha} = -K_{ij}^{\alpha\alpha'} u_j^{\alpha'}$. The bilateral symplectic algorithm, by Lapo Casetti [10], for time integrating these set of equations are given in Algorithm 1.

Algorithm 1 Bilateral symplectic algorithm

$(\mathbf{q}^0, \mathbf{p}^0) = (\mathbf{q}, \mathbf{p})\,|_t$
for $k = 1$ to n **do**
  $\mathbf{q}^k = \mathbf{q}^{k-1} + b^k \mathbf{p}^{k-1} \Delta t$
  $\mathbf{p}^k = \mathbf{p}^{k-1} - a^k \left(\nabla_q V\left(\mathbf{q}^k\right) - \mathbf{F}^{k-1}\right) \Delta t$
end for
for $h = n + 1$ to $2n$ **do**
  $\mathbf{p}^h = \mathbf{p}^{h-1} - b^{h-n} \left(\nabla_q V\left(\mathbf{q}^{h-1}\right) - \mathbf{F}^{h-1}\right) \Delta t$
  $\mathbf{q}^h = \mathbf{q}^{h-1} + a^{h-n} \mathbf{p}^{h-1} \Delta t$
end for
$(\mathbf{q}, \mathbf{p})\,|_{t+2\Delta t} = (\mathbf{q}^{2n}, \mathbf{p}^{2n})$

Here, n is the order of integration algorithm, $\mathbf{F}$ is external forcing if any involved, Δt is the time increment and k and h are iteration counters. The constants a^k and b^k up to forth order accurate methods are given in literature[9),8)]. The constants for forth order accuracy are $a_1 = a_4 = \left(2 + 2^{1/3} + 2^{-1/3}\right)/6$, $a_2 = a_3 = \left(1 - 2^{1/3} - 2^{-1/3}\right)/6$, $b_1 = 0$, $b_2 = b_4 = 1/\left(2 - 2^{1/3}\right)$ and $b_3 = 1/\left(1 - 2^{2/3}\right)$.

3. Problem Setting: Reported Experimental Observations of SWL and Details of Numerical Model

Using a laboratory shock wave lithotriptor and a set up for capturing high speed photoelastic images, Xi et al.[3] have recorded stress waves induced in different epoxy samples and crack patterns in a set of plaster of Paris samples. A brief overview of their experiments and results are explained at the beginning of this section while the problem setting and the numerical models are given in the latter part. For the sake of space saving, figures showing the observations made by Xi et al. are shown together with the numerical results in the next section.

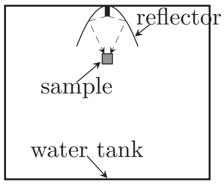

Fig. 3 Samples are kept at the focal point of the reflector, in a water filled tank.

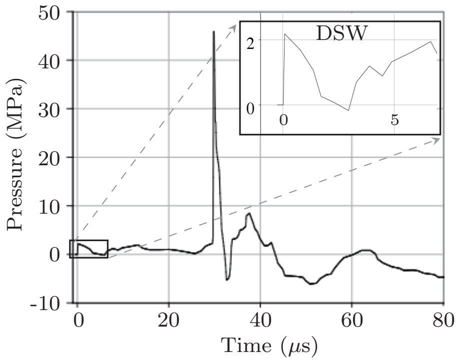

Fig. 4 Pressure wave form at the focal point. Enlarged is the Direct Shock Wave(DSW). Digitized from Xi et al.[3]

3.1 An overview of the experiment

In their experiments, Xi et al.[3] have used a laboratory electro-hydraulic shock wave lithotriptor which is similar to an unmodified HM-3 clinical lithotriptor. The shock wave generator was kept inside a water tank and the samples were kept at the focal point of the reflector (see Fig. 3). In addition to this basic set up, they have used a circular polariscope with bright field setting and high speed image capturing equipments to record the photoelastic fringe patterns of transient stress waves in various shaped and sized epoxy samples. Also, they have exposed various shaped and sized plaster of Paris samples to multiple lithotriptor shock waves and recorded the crack patterns.

Figure 4 shows the pressure wave form measured at the distal focal point of the reflector, where the samples are kept. This pressure wave form, made by digitizing the original wave form published by Xi et al.[3], is used as the input for the numerical simulations. There are two shock waves. The smaller shock wave, arriving first, is generated by an electrical spark at the proximal focal point of the reflector. This small amplitude spherical shock wave is called direct shock wave(DSW). Nearly $3\mu s$ after the DSW, a strong shock wave of peak stress 46.7MPa arrives. This is due to the focusing of large portion of the spherical shock wave at the distal focal point by the reflector, hence it's called focused shock wave(FSW). It's mentioned that the negative(tensile) portion of the pressure wave has not

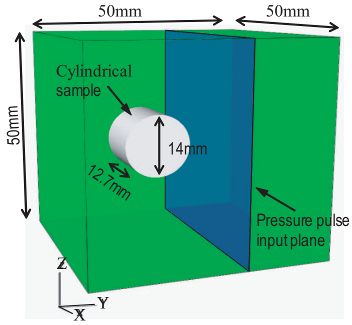

Fig. 5 Configuration of the numerical model

Table 1 Material properties.

	Epoxy	Plaster of Paris	Water
E /(GPa)	3.89	8.88	
K /(GPa)			2.2
ν	0.377	0.228	
ρ /(kgm^{-3})	1150	1670	1000
V_p /(ms^{-1})	2493	2478	1483
V_s /(ms^{-1})	1108	1470	–

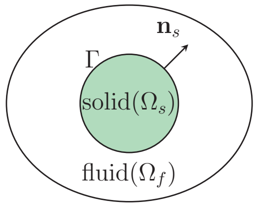

Fig. 6 Coupled solid and fluid domains. Γ is the wet boundary of the solid.

been well recorded due to the limitations of membrane hydrophones.

With various shaped and sized epoxy samples, they have recorded 3D photoelastic images of DSW and FSW induced transient stress waves. These 3D photoelastic fringe patterns had been used as an aid for understanding the complex interaction between the water shock wave and the solid samples. However, no quantitative information on the stress components can be extracted from these 3D photoelastic images; up-to-date, no method has been found to evaluate 3D stress distribution from 3D photoelastic images of sensitive photoelastic materials like epoxy[11). Also, they have reported the crack patterns in cylindrical and rectangular shaped plaster of Paris samples subjected to multiples shock waves. Out of these crack patterns, the most interesting is T-shaped crack surfaces of cylindrical samples, when the pressure wave incident angle is 90 degrees with the cylinder axis. This counter-intuitive crack pattern is a result of, shear shock/sub-shock waves, complex interference of reflected and incoming waves generating high stress regions, interaction of stress waves with extending crack surfaces, etc.. Main objective of this study is to simulate the observed T-shaped crack pattern so that some light can be shed on how the combination of above complex process initiate and drive cracks. For easy comparison and to save space, the experimental observations are presented with the numerical results in the next section.

3.2 Details of the numerical model

Three dimensional models have to be used in SWL related simulations since kidney stones, being comparable sizes in each dimension, experience 3D state of stress under the lithotriptor generated shock waves. Figure 5 shows the geometric details of the numerical model. The dimensions of the cylindrical sample are as same as those of the reported experiments; 14mm in diameter and 12.7mm in length. This sample was kept inside a 50mm × 50mm × 50mm domain filled with water. The dimension of the water domain is selected such that the effect of boundary reflections do not affect the transient stress field in the solid sample. Water is modelled with the linear elastic equation given in Eq. (1), since the deformation can be assumed infinitesimal. Shear modulus of water is assumed to be zero($\mu = 0$), since water does not support shear. Young's modulus(E), bulk modulus(K), Poisson's ratio(ν), density(ρ), P-wave velocity(V_p) and S-wave velocity(V_s) for epoxy[3)], plaster of Paris[12)] and water are given in Table 1.

According to Zhou et al.[2)], the profile of the water pressure pulse, especially the trailing part of the larger shock wave, has some difference in the vicinity of the sample. These changes are neglected and, assuming the incident shock wave to be plane, the pressure wave form in Fig. 4 is applied on a plane surface 2mm behind the cylindrical sample (see Fig. 5). Instead of the outermost boundary, the input pressure pulse is applied on an internal surface in order to reduce computation time.

To accurately model the pressure time history shown in Fig. 4 with linear PDS-FEM, very fine domain discretizations is necessary. Most important feature of this pressure time history is the peak pressure pulse of 2.7μs duration. The rise time of this pressure pulse is 32ns, which is too small to accurately model with linear elements for infinitesimal deformation. Hence, modelling of the peak pulse as a whole is taken into consideration. To this send, the solid cylinder and the its neighbourhood were modelled with finer elements. The number of total tetrahedral elements and degrees of freedom(DOFs) are 11.6 millions and 5.6 millions, respectively. It would be evident from the numerically calculated photoelastic patterns shown later, the mesh is refined enough to capture finer details like shear shock waves in the solid. To meet the large computations inherited with 3D models, a distributed parallel version of PDS-FEM was executed on a computer cluster with 128 CPUs.

3.3 Solid-fluid interaction

In this acousto-elastic problem, solid and fluid can be assumed to be in frictionless contact (slip condition). Under this assumption, kinematic condition requires that normal components of displacement of solid and fluid domains should be equal at the shared boundaries (i.e. solid-fluid interface). Also, the kinetic condition requires that the normal traction of the two domains should be balanced on the solid-fluid interface and no shear traction is transferred between the two domains via the solid-fluid interface. Denoting the solid and fluid domains with Ω_s and Ω_f(see Fig. 6) , respectively, and the interface boundary with Γ, the kinematic and kinetic conditions can be written as;

$$\begin{aligned} \left(\mathbf{u}_f - \mathbf{u}_s\right).\mathbf{n}_s &= 0 \text{ kinematic condition} \\ \sigma_n + p_f &= 0 \text{ kinetic conditions} \\ \boldsymbol{\sigma}_t &= \mathbf{0}, \end{aligned} \tag{5}$$

where $\mathbf{n}_s$ is the normal vector to the wet boundary of the solid($\partial\Omega_s \cap \Gamma$). $\mathbf{u}_s$ and $\mathbf{u}_f$ are the displacements of solid and fluid on Γ (on $\partial\Omega_s \cap \Gamma$ and $\partial\Omega_f \cap \Gamma$). p_f is the water pressure and $\boldsymbol{\sigma}_s$ is the stress tensor in solid domain. $\sigma_n = \mathbf{n}_s.(\boldsymbol{\sigma}_s.\mathbf{n}_s)$ is the normal stress and $\boldsymbol{\sigma}_t = \boldsymbol{\sigma}_s.\mathbf{n}_s - \sigma_n\mathbf{n}_s$ is the tangential traction vector on Γ. $\boldsymbol{\sigma}_t = \mathbf{0}$ on Γ is usually called slip condition.

The above solid-fluid interface conditions were implemented with a partitioned approach which leads to weak coupling. In partitioned approaches[13], instead of solving a monolithic problem, the solid and fluid domains are solved separately and their interaction is modelled by imposing above kinetic and kinematic conditions on Γ after each time update. Strong coupling of two domains with implicit methods is stable, but numerically intensive especially for problems involving large DOFs. We implemented weak coupling of two domains with simultaneous enforcing conditions given by Eq. (5) on the solid-fluid interface, as shown in the Algorithm 2.

Algorithm 2 Bilateral symplectic algorithm with weak solid-fluid interaction

$(\mathbf{q}^0, \mathbf{p}^0) = (\mathbf{q}, \mathbf{p})\,|_t$
for $k = 1$ to n **do**
  update SF interface conditions
  $\mathbf{q}^k = \mathbf{q}^{k-1} + b^k\mathbf{p}^{k-1}\Delta t$
  $\mathbf{p}^k = \mathbf{p}^{k-1} - a^k\left(\nabla_q V\left(\mathbf{q}^k\right) - \mathbf{F}^{k-1}\right)\Delta t$
end for
for $h = n + 1$ to $2n$ **do**
  update SF interface conditions
  $\mathbf{p}^h = \mathbf{p}^{h-1} - b^{h-n}\left(\nabla_q V\left(\mathbf{q}^{h-1}\right) - \mathbf{F}^{h-1}\right)\Delta t$
  $\mathbf{q}^h = \mathbf{q}^{h-1} + a^{h-n}\mathbf{p}^{h-1}\Delta t$
end for
$(\mathbf{q}, \mathbf{p})\,|_{t+2\Delta t} = (\mathbf{q}^{2n}, \mathbf{p}^{2n})$

Each update of solid-fluid interface conditions involves the following two steps.

1. calculate fluid pressure and update $\mathbf{F}^{k-1}$ on $\partial\Omega_s \cap \Gamma$ such that kinetic conditions are satisfied
2. update $\mathbf{q}^{k-1}$ on $\partial\Omega_f \cap \Gamma$ such that kinematic conditions are satisfied

Usually, in solid-fluid interaction problems, the meshes of solid and fluid domains are not conforming at the interface and interpolations of pressure and displacements are required in implementing the above interface conditions. The deformation involved in this acousto-elastic problem is infinitesimal. Therefore, overhead of interpolations is avoided by using conforming meshes at the solid-fluid interface.

4. Results of Numerical Simulations

In this section, results of numerical simulations are presented. First the stress waves induced in a epoxy sample due to DSW and corresponding 3D photoelastic images are presented as a qualitative evaluation of the numerical results. Next, the necessity of dynamic fracture criterion is explained. The numerically simulated crack patterns and experimentally observed by Xi et al. are qualitatively and quantitatively compared, in the latter part.

4.1 DSW Induced Stress Waves and Photoelastic Images of Epoxy Samples

As a qualitative verification, numerically computed photoelastic images are compared with that of the experimentally observed by Xi et al.. Quantitative comparisons of stress filed or photoelastic fringe patterns are not possible due to lack of information. Only the static photoelastic constant for the epoxy samples used in the experiment is known[3]. Usually, the dynamic photoelastic constant is 10% to 30% is higher than that of the static. As it was mentioned in section 3.1, the tensile phase of the lithotriptor shock waves are poorly recorded, due to the limitations of membrane hydrophones used in the experiment. Only a qualitative comparison is possible with these limitations.

Some snap shots of the principal stress and maximum shear stress of epoxy sample under DSW are shown in Fig. 7 and 8. Since $V_p^E > V_p^W$, where W and E stand for water and epoxy, the induced P-wave in epoxy diverges and moves ahead. This diverging P-wave front induces a shock wave in water, which is clearly visible in Fig. 7. In addition, this diverging P-wave induces shear shock wave at the solid-fluid interface. Another shear shock wave is induce in epoxy samples since $V_p^W > V_s^E$. Both the diverging solid P-wave and lithotriptor shock wave induced shear shock waves are clearly visible in both the figures. In both figures, small arrows are pointing to some of the shear shock waves.

3D photoelastic images, corresponding to that of experimentally observed, are numerically computed for the cylindrical epoxy sample under DSW. For the photoelastic image generation, the governing equation of photoelasticity[14] was numerically integrated along a

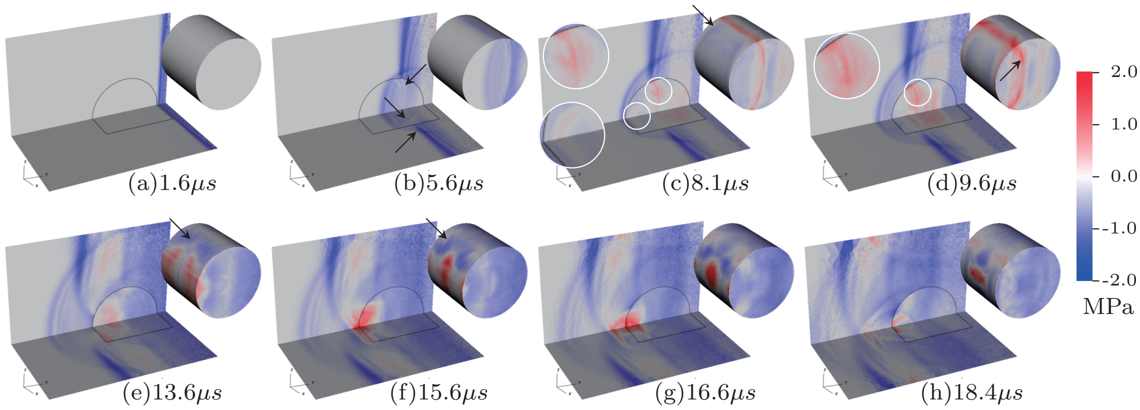

Fig. 7 Maximum principal stress of epoxy sample under DSW. Horizontal and vertical sections of the model and the surface of the cylinder are shown. Note the shock waves in the solid and water.

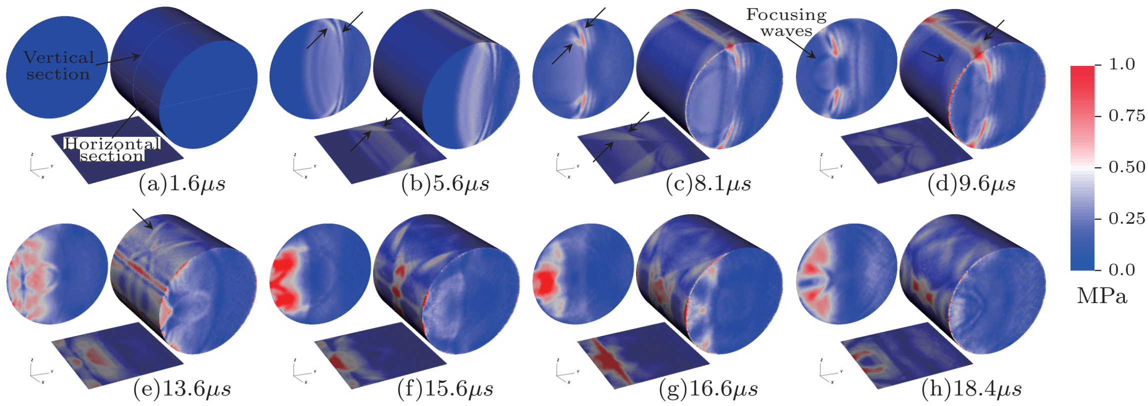

Fig. 8 Maximum shear stress of epoxy sample under DSW. Horizontal section, vertical sections and the surface of the cylinder are shown. Note the shear shock waves.

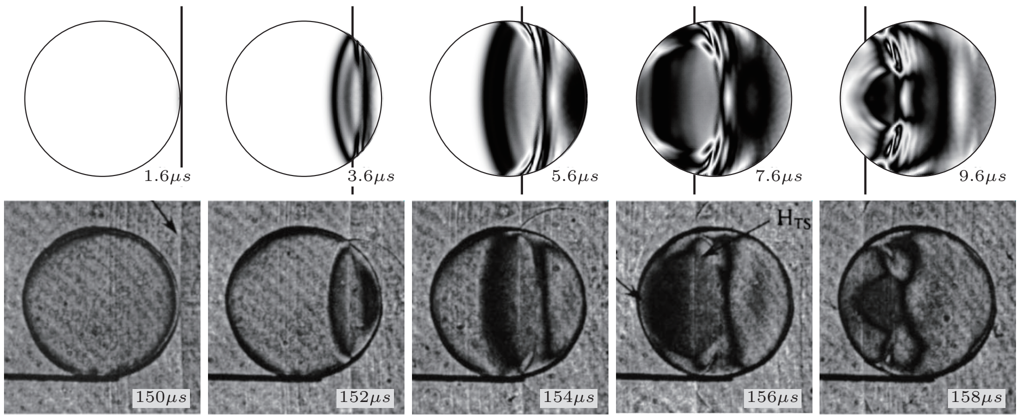

Fig. 9 Numerical and experimental photoelastic images at $2\mu s$ intervals, for the epoxy cylinder under DSW. Source of the experimental images in the bottom row is Xi et al.[3].

dense set of light rays passing through the cylindrical sample, parallel to its axis. The governing equation of photoelasticity can be written in terms of light vector components $\left\{A_x,\ A_y\right\}^T$, stress components, σ_{xx}, σ_{xy} and σ_{yy}, in a plane normal to the light propagation direction z and the photoelastic constant C_0 for the given material as;

$$\frac{d}{dz}\left\{\begin{array}{c} A_x \\ A_y \end{array}\right\} = \frac{-\iota C_0}{2}\left[\begin{array}{cc} \sigma_{xx}-\sigma_{yy} & 2\sigma_{xy} \\ 2\sigma_{xy} & \sigma_{yy}-\sigma_{xx} \end{array}\right]\left\{\begin{array}{c} A_x \\ A_y \end{array}\right\}.$$

As seen in Fig. 9, the numerically computed photoelastic images match well with that of the experimentally obtained. The fore-mentioned diverging P-waves and the

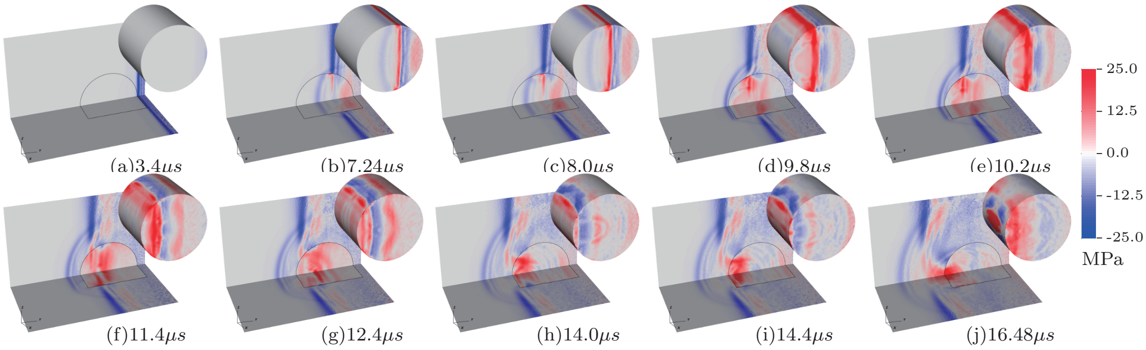

Fig. 10 Maximum principal stress in plaster of Paris samples.

two shear shock waves are easily identifiable in both the image sets. Some differences in the last set of images are mainly attributed to the lack of dynamic photoelastic constant and the poor sensitivity of membrane hydrophones to tensile phase. Irrespective, of these limitations the two image sets closely match qualitatively validating the numerical model.

It should be noted that the photoelastic images shown in Fig. 9 carry integrated information of the 3D state of stress induced in the cylindrical sample(Fig. 7 and 8). The inverse problem of 3D photoelasticity is still unsolved for sensitive materials like epoxy due to its non-linear and ill-posed nature[11]. State of stress cannot be inferred from these images even qualitatively.

4.2 Stress waves in Plaster of Paris under FSW

Figure 10 shows the evolution of stress waves in plaster of Paris under FSW. Being the shear wave speed(V_s^P) slightly lower than V_p^W, water pressure wave does not induce a shear shock wave in plaster of Paris. Still, the amplitude of this shear wave is large since $V_s^P \approx V_p^W$. This large amplitude shear wave is clearly visible in Fig. 10 (*b*) to (*g*) as a planner red colour strip. Once these, high amplitude wave front reaches the distal circular surface, some portion of its energy is transferred to water and the rest reflects and focus. When the waves reflect, their phases change. This focusing of the phase changed reflected wave and the constructive interference with the incoming waves create high stress regions as seen in Fig. 10 (*d*) to (*j*). Especially, in Fig. 10 (*g*) a localized high stress region parallel to the cylinder axis is visible. The location of this region matches with the location of the vertical crack of the T-shaped crack described at the latter part of this section.

4.3 Need of a Dynamic Fracture Criterion

As seen in Figs. 10 (*b*) to (*f*), the sub-shock shear wave generates above 25MPa tensile stress in the sample. After reflecting from the distal surface, focusing and interference with the incoming waves generate maximum tensile stress above 40MPa. These values are several times larger than the static tensile strength of plaster of Paris, which is around 4 and 6MPa. In addition, the maximum strain rate is above 8×10^3 according to Fig. 11. Both these localized high stresses and high strain rates indicate that dynamic failure criterion has to be used in SWL simulations.

4.4 Dynamic Failure Criterion

When subjected to dynamic loading, the crack propagation is strongly depends on strain rate, stress wave amplitude and the exposure time[15),16),17)]. Due to its simplicity in implementation, Tuler-Butcher criterion is used in this study. The Tuler-Butcher failure criterion [15),16),18)] can be expressed as

$$\int_0^{t_f} (\sigma_1 - \sigma_0)^\beta dt \geq K_f, \tag{6}$$

for $\sigma_1 \geq \sigma_0 \geq 0$ where $\sigma_1$is the maximum principal stress, σ_0 is a specific threshold stress, t_f is time for the fracture and K_f is the stress impulse for failure. Since experimental information on the values of β, t_f, σ_0 and K_f for the material of interest are not available, we assumed $\beta = 2$ and $\sigma_0 = 15MPa$ while $K_f = 100 \times 10^{-6}$ MPa$^2\mu s$. With this failure criterion, we could reproduces the T-shaped crack patterns in plaster of Paris samples, observed by Xi et at. Even with $K_f = 50 \times 10^{-6}$ MPa$^2\mu s$, the same T-shaped crack pattern was observed. However, it should be emphasized that Tuler-Butcher criterion could not be the best and better dynamic failure criterion are to be sought in future studies.

4.5 Comparison of Numerically and Experimentally Obtained Crack Patterns.

When exposed to multiple pressure pulses, Xi et al. have observed that cylindrical samples of various sizes have broken into three parts with T-shaped crack profiles. The experimentally observed T-shaped crack profiles are shown in Fig. 12. Just as observed in the experiment, when exposed to multiple pressure pulses, the cylindrical sample of the numerical simulation broke into three parts with T-shaped crack profiles. Fig. 13 shows the crack profile of the numerical simulation at several sections. The number at the bottom right of each sub-figure indicates the distance from the centre of the cylinder (+ and − stands for the left and right). As shown in Fig. 14, the vertical crack of the numerically obtained crack profile is located almost at the same place observed in the experiment. This indicates that numerical crack profile is in good agreement with the experimental observations, quantitatively.

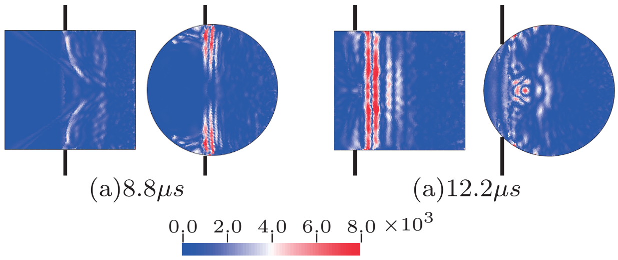

Fig. 11 Maximum strain rate of plaster of Paris sample, along a horizontal and vertical sections.

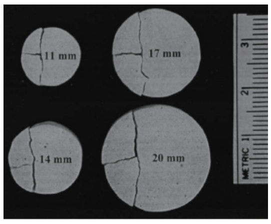

Fig. 12 T-shaped cracked plaster of Paris samples (source Xi et al.[3])

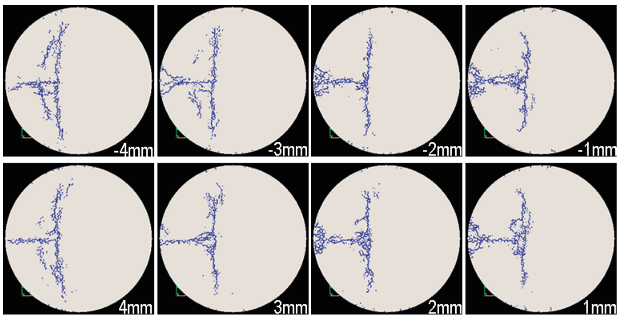

Fig. 13 Numerically simulated crack patterns. The number stands for the distance from the centre.

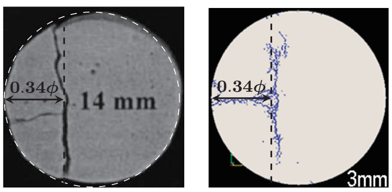

Fig. 14 Comparison of the location of the vertical crack surface. ϕ is the diameter of the cylinder

5. Summary and concluding remarks

Numerical reproduction of some experimental observations, including 3D dynamic crack propagation, related to SWL are presented in this paper. SWL related stress wave and crack propagation simulations requires fine domain discretization for accurately modelling the shock waves. Especially, accurately modelling the shear shock/sub-shock waves induced in solid is important as those play a key role in fragmenting the stone. To simulate this crack propagation phenomena requiring multi-million degrees of freedom, PDS-FEM is used since it provides simple and numerically efficient failure treatments. As it is shown, the numerically generated photoelastic images are qualitatively in agreement with that of the experiment while the numerically obtained crack patterns are quantitatively in agreement with that of the experiment. These results indicates the potentiality of PDS-FEM to simulate complex 3D crack propagation phenomena that require large scale computations. Further, PDS-FEMs ability to model crack propagation in heterogeneous materials is useful in SWL simulations since kidney stones are highly heterogeneous. In future, detailed study of the sources of crack initiation and driving, time and spatial distribution of lithotriptor shock waves for efficiently breaking the kidney stones, etc. are to be conducted.

Acknowledgments

The authors gratefully acknowledge the financial support from the Japan society for the promotion of science and the ministry of education, culture, sports, science and technology (grant number 21710183).

REFERENCES

1) Robin O. Cleveland and Oleg A. Sapozhnikov, Modeling elastic wave propagation in kidney stones with application to shock wave lithotripsy, *J. Acoust. Soc. Am.*, Vol.118(4), pp.2668-2676, 2005.
2) Yufeng Zhou and Pei Zhong, The effect of reflector geometry on the acoustic field and bubble dynamics produced by an electrohydraulic shock wave lithotripter, *J. Acoust. Soc. Am.*, Vol.119(6), pp.3625-3636, 2002.
3) Xufeng Xi and Pei Zhong, Dynamic photoelastic study of the transient stress field in solids during shock wave lithotripsy, *J. Acoust. Soc. Am.*, Vol.109(3), pp.1226-1239, 2001
4) Oleg A. Sapozhnikov, Adam D. Maxwell, Brian MacConaghy, and Michael R. Bailey, A mechanistic analysis of stone fracture in lithotripsy, *J. Acoust. Soc. Am.*, Vol.121(2), pp.1190- 1202, 2007.
5) Hori M, Oguni K, Sakaguchi H, Proposal of FEM implemented with particle discretization for analysis of failure phenomena, *Journal of Mechanics and Physics of Solids*. Vol.53-3, pp.681-703, 2005.
6) M. L. L. Wijerathne , Kenji Oguni and Muneo Hori,

Numerical analysis of growing crack problems using particle discretization scheme, *Int. J. for Numerical Methods in Eng.*, DOI 10.1002/nme.2620, Vol.80, pp.46-73, 2009

7) A. Lew, J. E. Marsden, M. Ortiz & M. West, Asynchronous variational integrators. *Arch. Ration. Mech. Anal.*, Vol.167-2, pp.85-146, 2003.
8) Candy, J. and R. Rozmus, A Symplectic Integration Algorithm for Separable Hamiltonian Functions, *J. Comput. Phys.*, Vol.92, pp.230-256, 1991.
9) Forest E. and Ruth R. D., Fourth-order symplectic integration, *Physica D: Nonlinear Phenomena*, Vol.43-1, pp.105-117, 1990.
10) Lapo casetti, Efficient symplectic algorithm for numerical simulation of Hamiltonian flows, *Physica scripta*, Vol.51, pp.29-34, 1994.
11) M.L.L. Wijerathne, K. Oguni and M. Hori (2008) Stress field tomography based on 3D photoelasticity, *Journal of the Mechanics and Physics of Solids*, Vol.56-3, pp.1065-1085, 2008.
12) Yunbo Liu and Pei Zhong, BegoStone—a new stone phantom for shock wave lithotripsy research, *J. Acoust. Soc. Am.*, Vol.112(4), pp.1265-1268, 2002.
13) C. Felippa, K. Park, C. Farhat, Partitioned analysis of coupled mechanical systems, *Computer Methods in Applied Mechanics and Engineering*, Vol.190, pp.3247-3270, 2001.
14) Aben, H., *Integrated photoelasticity*, McGraw-Hill, New York, 1977.
15) J. Jeong, H. Adib and G. Pluvinage, Proposal of new damage model for thermal shock based on dynamic fracture on the brittle materials, *Journal of Non-Crystalline Solids*, Vol.351 24-26, pp.2065-2075, 2005.
16) A. Nyoungue, Z. Azari, M. Abbadi, S. Dominiak and S. Hanim (2005), Glass damage by impact spallation, *Materials Science and Engineering*, Vol.407 1-2, 25, pp.256-264, 2005.
17) V.E. Fortov, D. Batani, A.V. Kilpio, I.K. Krasyuk, I.V. Lomoosov, P.P. Pashinin, E.V. Shashkov, A.Y.U. Semenov, and V.I. Vovchenko, The spall strength limit of matter at ultrahigh strain rates induced by laser shock waves, *Laser and Particle Beams*,Vol.20, pp.317-320, 2002.
18) Z. F. Zhang,a F. F. Wu, W. Gao, J. Tan, and Z. G. Wang, M. Stoica, J. Das, and J. Eckert , B. L. Shen and A. Inoue, Wavy cleavage fracture of bulk metallic glass, *Applied Physics letters*, Vol.89, 2006.

(Received 2010, March 9)